TRANSPORT MECHANISMS IN POROUS FINS

Filippo Coletti
Dept. Mechanical Engineering
Stanford University
Stanford, California, USA
colettif@stanford.edu

Kenshiro Muramatsu
DENSO Corporation
1-1 Showa-cho, Kariya, Aichi, Japan
KENSHIRO_MURAMATSU@denso.co.jp

Daniele Schiavazzi
Mechanical & Aerospace Engineering
University of California, San Diego
La Jolla, California, USA
dschiavazzi@eng.ucsd.edu

Chris J. Elkins
Dept. Mechanical Engineering
Stanford University
Stanford, California, USA
celkins@stanford.edu

John K. Eaton
Dept. Mechanical Engineering
Stanford University
Stanford, California, USA
eatonj@stanford.edu

ABSTRACT

Lotus-type fins are a class of porous metal foam having high aerothermal performance. We investigate the flow and scalar transport through a set of such fins by means of MRI-based velocimetry and concentration measurements. For compatibility with the measurement technique, magnified 3D-printed replicas are utilized, with water-based solutions as the working fluid. The choice of geometric parameters (fin spacing and thickness, porosity, and hole diameter) is based on previous thermal studies. The Reynolds number based on the mean pore diameter and inner velocity ranges from Re=80 to 3800. The velocity and vorticity fields show the formation of elongated jets, which impact on the successive fin, producing interacting wall-jets and eventually streamwise swirling motion. The random hole distribution causes the time mean streamlines to meander in a random-walk manner. The mechanical dispersion associated with this is evaluated using the 3D velocity data. Overall the flow measurements suggest that a change in regime occurs around Re=290, and we hypothesize that this coincides with the inception of unsteady/turbulent motion. This is supported by the measurements of concentration of an isokinetic non-buoyant plume of scalar injected upstream of the stack of fins. The diffusion of scalar away from the injection point is significantly faster for Re>290.

INTRODUCTION

Metal foams are increasingly used in heat exchangers because they provide large surface area and high heat transfer coefficient while being compact and lightweight. Unfortunately our understanding of the flow physics and heat transport within their complex structures is far from complete, due to the difficulty of performing accurate simulations and detailed measurements. In several relevant applications the flow regimes extend well beyond the limits of applicability of Darcy's Law (negligible inertia forces) and Forchheimer's Law (laminar flow). Flows in porous media typically start to develop turbulent eddies at Reynolds numbers based on the pore diameter of about 150 to 300 (Vafai et al., 2006). The available analytical models do not provide satisfactory solutions in this regime.

A class of metal foam which has very useful properties for heat exchanger applications is made from lotus-type porous metal (Nakajima et al., 2010). Lotus-type porous metal has elongated pores of random size and spatial distribution but a common orientation. Sets of lotus fins are obtained by slicing the metal into thin layers normal to the pores and stacking them in the flow path, forcing the fluid to pass through the pores (Fig. 1). Lotus fins represent a promising alternative to conventional metal foam heat exchangers because they offer higher thermal conductivity and lower pressure drop (Muramatsu et al., 2012). Analysis of a set of lotus fins requires understanding of the mechanisms that transport a passive scalar (concentration or temperature) normal to the main flow direction. We have used Magnetic Resonance Imaging (MRI) to analyze the fluid flow and scalar dispersion through lotus fins, in order to determine its transport properties in a range of flow regimes.

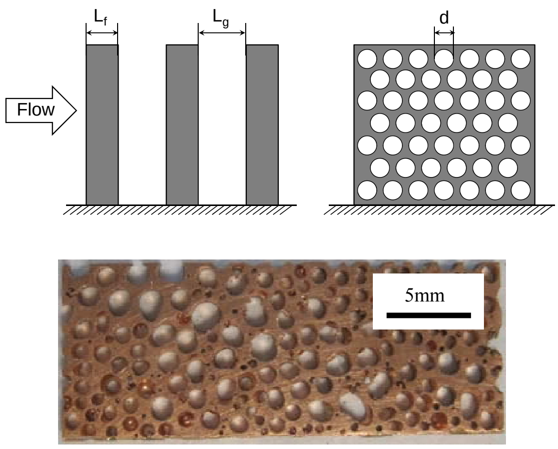

Figure 1. Top: schematic representation of lotus-type fins with characteristic geometrical parameters. Bottom: an actual copper lotus-type fin.

METHODOLOGY

Porous fin configuration

Geometric parameters for the present investigation were chosen based on the experience gained in our recent study of the aero-thermal performance of lotus fins (Muramatsu et al. 2012), and on the work of Chiba et al. (2011). Muramatsu et al. determined the heat transfer and pressure drop characteristic of stacks of fins with deterministic and random hole distributions. Both porosity and inter-fin spacing were varied. Porosity ranged between φ = 0.28 and φ = 0.7, with the best performance obtained at φ = 0.6. The inter-fin gap L_g varied between zero and $4L_f$, where L_f is the fin thickness (see Fig. 1 for the definition of the geometric parameters). At low spacing, the heat transfer enhancement due to jet impingement comes at the expense of a higher pressure drop. However this penalty was marginal for $L_g \geq L_f$. A porosity of 0.6 and a spacing $L_g = L_f$ thus is a realistic design choice.

Chiba et al. (2011) showed that the aerothermal performance improves with decreasing fin thickness, for the same porosity and pore size. This is due to the thin thermal boundary layer and the limited friction inside the pores. The lower limit in terms of fin thickness is imposed by the manufacturing capabilities and the mechanical robustness of the final specimen. Chiba et al. (2011) tested a minimum thickness of 1 mm, with a mean pore diameter about 0.57 mm and a porosity of 0.6.

Based on the above considerations, we chose values of the geometric parameters that are optimal for the fin performance and representative of common configurations of technological interest: the mean pore diameter is d = 0.55 mm, the porosity φ = 0.6, the pore depth (equal to the fin thickness) L_f = 1.0 mm, and the gap between the fins L_g = 1.0 mm. A random hole distribution was generated for each fin by a numerical routine, following the hole size pdf investigated by Chiba et al. (2011).

Apparatus and flow conditions

Three component velocity measurements were obtained for a 9X scaled up model of a lotus-metal fin set mounted in a duct. The scaled porous fins had a mean hole diameter of d = 4.95 mm, Lf = 9.0 mm, and Lg = 9.0 mm. The porosity of the individual fin elements remains ϕ = 0.6. A set of eight fins was mounted in a 50 mm square by 135 mm long duct as illustrated in Figure 2. The entire fin set and channel were built as a single unit using stereolithography. The lotus fin test section is mounted in a water tunnel (Fig. 3) that includes upstream flow conditioning sections and a contraction to obtain good flow uniformity at the test section inlet.

A ½ HP magnetic drive centrifugal pump (Little Giant, TE-5.5-MD-HC) circulated the fluid from a reservoir through the test section and back to the reservoir. The mass flow rate was measured by a paddle wheel flow meter with an estimated uncertainty of 2%.

A wide range of flow regimes was investigated by varying the mean bulk flow velocity and the viscosity of the working fluid. The latter is adjusted by adding glycerine (up to 50% by weight) to deaerated water. This is needed to keep the minimum bulk flow velocity above 0.1 m/s, in order to achieve optimal velocity measurement accuracy Copper sulfate at a concentration of 0.05 mol/L is added to the fluid in order to increase the MRI signal-to-noise ratio.

Defining the Reynolds number based on the mean hole diameter and the inner velocity (equal to the incoming bulk velocity divided by the fin porosity), the tested regimes range between Re=80 and Re=3800. Table 1 summarizes the flow conditions for the MRI velocity measurements.

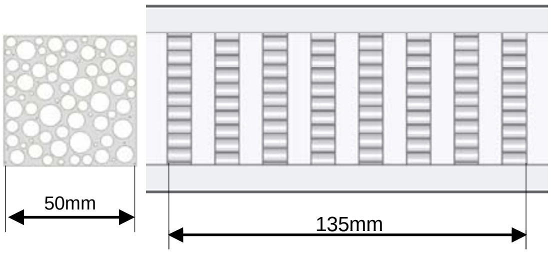

Figure 2. Frontal view and lateral view of the lotus fin set.

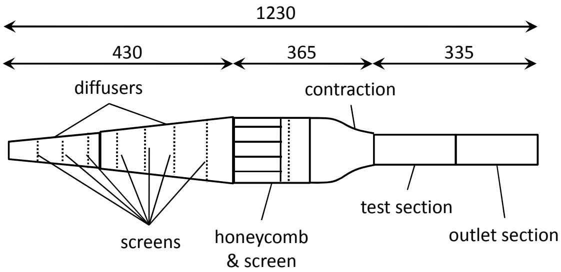

Figure 3. Schematic of the water tunnel.

Table 1. Fluid and flow properties for the various tested regimes during MRI velocity measurements. Viscosity is measured with a viscometer.

Re [-]	Viscosity [m^2s^{-1}]	Bulk velocity [ms^{-1}]
80	$2.1 \cdot 10^{-5}$	0.2
145	$5.9 \cdot 10^{-6}$	0.1
190	$7.4 \cdot 10^{-6}$	0.17
240	$7.4 \cdot 10^{-6}$	0.22
290	$5.9 \cdot 10^{-6}$	0.21
458	$5.9 \cdot 10^{-6}$	0.33
1860	$1 \cdot 10^{-6}$	0.26
3800	$1 \cdot 10^{-6}$	0.46

During the scalar transport measurements an isokinetic plume of non-buoyant contaminant was injected into the flow along the centerline, 9 mm upstream of the front face of the first fin. In order to minimize the wake of the injection device, a 2 mm thick NACA0012 airfoil-shaped strut was inserted in the duct, spanning the entire height. The strut (represented in Fig. 4) is provided with a cylindrical internal passage (0.7 mm in diameter) running along its span. The cavity makes a 90 degree bend and exits through a tube which extends 10 mm beyond the trailing edge. The device is manufactured in one piece by SLA. Figure 5 shows a 3D view of the fin set and the passage for scalar injection (the strut is hidden for clarity).

The main flow is water for the scalar measurements and the injected scalar is a solution of copper sulfate in water (0.075 mol/L). The copper sulfate has a strong MRI signal so the meandering and spreading plume can be accurately tracked. The copper sulfate increases the fluid density, which would result in a negatively buoyant plume. This was offset by adding ethyl alcohol (7% in volume) to the injected fluid. The MRI measurements show no significant buoyancy in the plume.

A syringe pump (KD scientific, model 100) supplied copper sulfate solution to the injection tube at a precisely metered flow rate. Special attention is paid to avoid injection of air bubbles, which would show as artifacts in the MRI reconstruction.

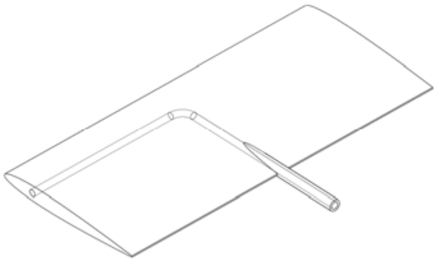

Figure 4. Device for the injection of passive scalar.

Measurement technique

MRI Experiments were performed at the Richard M. Lucas Center for Magnetic Resonance Imaging at Stanford. A 3 Tesla General Electric whole body scanner was utilized, with a standard transmit-and-receive radio-frequency coil commonly used for imaging human heads. A flip angle of 55 degrees and a bandwidth of 62.5 kHz are used. Velocity data were obtained using the method of magnetic resonance velocimetry (MRV) described by Elkins et al. (2003). Three-component velocity measurements were obtained on a uniform Cartesian grid at a resolution of 0.6 mm. The acquisition process took several minutes, so the acquired velocity fields are time-averaged. Typical uncertainties for the local velocity components are about 5%, although higher errors are possible close to solid boundaries due to partial volume effects (i.e. the presence of both fluid and SLA resin in a near-wall voxel).

The scalar concentration measurements were done using the Magnetic Resonance Concentration (MRC) technique developed by Benson et al. However, the copper sulfate concentration at plume injection is approximately 5X higher than used previously to maximize the dynamic range of the measurements. This is required in this application because of the very low concentration levels expected in the plume at downstream stations. The high concentration at injection allows MRC measurements at concentrations below 5% of injection concentration. However, the uncertainty in the absolute concentration value is significantly larger than with standard MRC techniques.

RESULTS

In the presentation of the data, velocity and distance are normalized by the inner velocity U_{in} and the (average) hole diameter d, respectively. X denotes the streamwise direction and Y and Z denote the transverse directions. The origin of the coordinate system is located on the channel centerline, at the front face of the first fin.

Mean flow features

The general features of the velocity fields are shown in Fig. 6. Streamwise cuts along the centerline of the test section are shown for Re = 145. It is evident that some jets stream directly through several fins without significant impacts on the perforated walls. On the other hand the random structure of the solid web occasionally creates points of large blockage, resulting in extended regions of reverse flow. The tangle of long jets and large flow reversals is suggestive of a chaotic flow pattern, although frozen in time.

The bottom panel of Fig. 6 presents a transverse plane 0.3d upstream of the 6th fin, a location where any entry effect has long disappeared. In-plane velocity vectors are superimposed on color contours of streamwise velocity, and the fin structure is overlaid in translucency. The jets issued by the 5th fin are visible, and impinge on the solid web of the 6th fin. The jets have a large range of size and intensity, and are arranged in a dense array without any geometrical symmetry. Therefore the wall jets generated at the impingement locations interact with wall jets of possibly different intensity and orientation, leading to areas of significant shear along the transverse plane. This mechanism appears to generate intense secondary flow motions in the vicinity of the hole inlets. It will be shown that streamwise vortical motions persist through the fin and in the jets emerging out of the holes. This observations hold for all investigated Reynolds numbers.

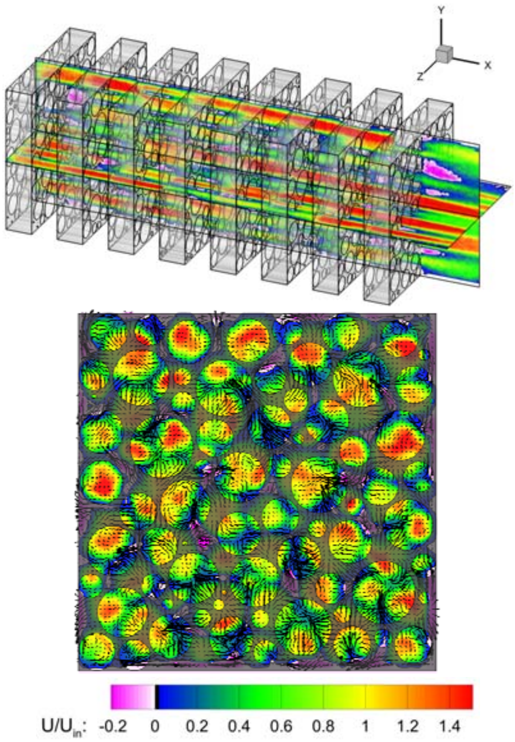

Figure 6. Top: Streamwise cuts through the centerline, with contours of streamwise velocity. Bottom: in-plane velocity vectors overlaid to contours of streamwise velocity at 0.3d upstream of the 6th fin front face.

Vorticity field

Streamwise vorticity is associated with transverse mixing and therefore plays an important role in the transfer properties of the lotus-type fins. Vorticity is calculated by differentiation of the velocity field using a second-order central difference scheme. Figure 7 displays isosurfaces of positive and negative streamwise vorticity ($\omega_X = 0.2U_{in}/d$ in red, $-0.2U_{in}/d$ in blue) for Re=145, 290 and 458. Intense, long-lived streamwise vortices extend throughout the larger holes, and sometimes reach the following fin. The vortical structures are generated just upstream of each fin, supporting the view that the origin of the streamwise swirling motions are due to the impingement of randomly distributed jets on a random solid web, generating a braid of colliding wall jets of various orientations and intensities. The wall jets' interaction on the YZ plane produces swirl along the X axis (see Fig. 6). The vortices are then accelerated into the holes, further increasing their angular velocity.

Interestingly, the intensity and extent of the vortices does not vary monotonically with the Reynolds number. Looking at all tested regimes, the strength of the stream wise vortical structures increases up to Re=290, but is reduced for higher flow regimes. This suggests that, between Re = 290 and Re = 458, the flow regime changes from mostly laminar to unstable/turbulent. Consequently the coherence of the mean vorticity pattern is partially disrupted.

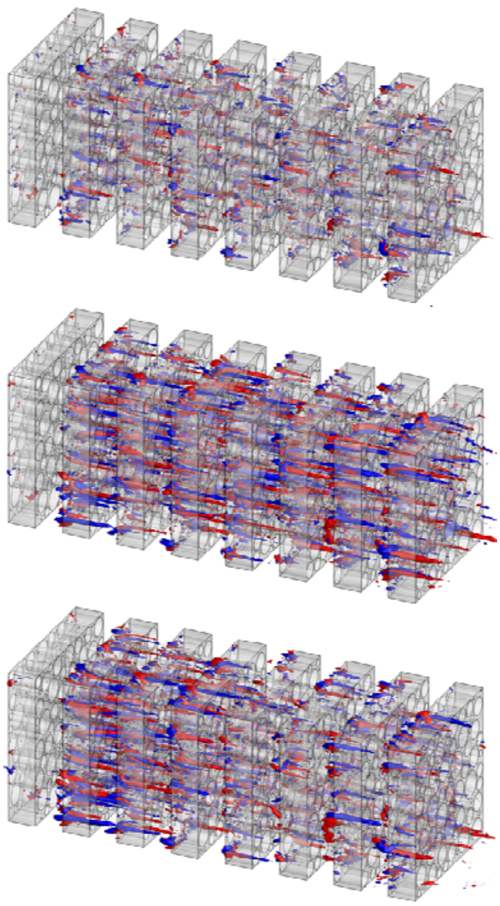

Figure 7. Isosurfaces of positive and negative streamwise vorticity at Re = 145 (top), 290 (center) and 458 (bottom).

Mechanical Dispersion

The 3D velocity fields can be used to investigate the mechanical dispersion caused by the porous fins. Mechanical dispersion is the spreading imposed by the fin structure, which causes nearby fluid parcels to follow diverging paths (Saffman, 1959; Koch and Brady, 1985). In random configurations, the mechanical dispersion is caused by the stochastic velocity field, and is therefore a function of both geometry and flow regime. In the present case, although the randomness in the streamwise direction is removed by the regularity of the fin spacing, mechanical dispersion is induced by stochastic transverse fluid motion through randomly distributed holes.

The mechanical dispersion coefficient for the lotus fins is determined following the method developed by Onstad et al. (2011), who performed a streamline displacement analysis of the velocity field through an open-cell foam. To calculate the streamlines, the open-source post-processing and visualization software package ParaView is used. Given a starting point and the velocity field, a stream-trace (i.e. the path of a mass-less particle in the vector field) is calculated by an adaptive integration algorithm (Runge Kutta 4th order). 2500 streamlines are computed starting from a section 9 mm upstream of the first lotus fin, up to the rear face of the last lotus fin. The starting points are distributed on a Cartesian grid with a uniform spacing of 0.6 mm. The grid covers the 30 mm x 30 mm core of the fluid volume, so that no streamline is started closer than 10 mm from any sidewall. The streamlines which do not pass through the entire set of lotus fins are discarded.

The rms streamline displacement σ in the YZ plane is calculated as a function of the superficial time t_s. The latter is the distance travelled by a fluid parcel divided by the inner velocity in the lotus fins. The mechanical diffusivity D_M, which is expressed by Eq. (1), is determined by finding the best fit linear slope in the diagram $\sigma = \sigma(t_s^{0.5})$ for the region after the third fin, where the standard deviation increases as the square root of the superficial velocity (long-time behavior):

$$D_M = \frac{\sigma^2}{2t_s} \tag{1}$$

The calculated values of mechanical diffusivity for all investigated cases are plotted in Fig. 8, where they are normalized by the kinematic viscosity ν. Even at the smallest Reynolds numbers, the mechanical dispersion is much larger than the molecular dispersion, indicating that it can play a significant role in the heat/mass transport. It is apparent that a qualitative change takes place in the mechanical dispersion mechanism between Re = 290 and 458. This is consistent with a transition from laminar to unstable/turbulent flow, as inferred in the previous sections. In particular, the diminished growth rate of D_M

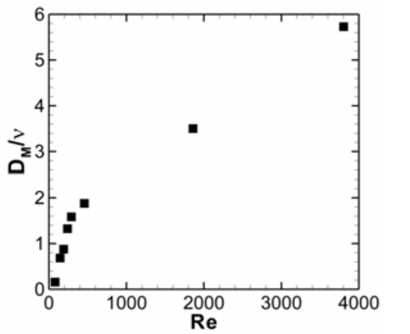

Figure 8. Mechanical dispersion coefficients (normalized by kinematic viscosity) versus Reynolds number,

above Re = 458, agrees with the observation that the large structures of mean streamwise vorticity are disrupted by turbulent agitation, limiting the mechanical transverse mixing (in the mean flow sense).

Scalar concentration measurements

Figure 9 displays a 2.5% scalar concentration isosurface for Re = 145, 290, 458 and 1860. The concentration is calculated by normalizing the local signal magnitude by the maximal signal magnitude at the injection point. As mentioned above, the absolute value of concentration is affected by significant uncertainty. However, the purpose here is to compare the relative difference in the patterns at various flow regimes.

The plume issuing from the injector meanders through the random hole distribution. In general, three main mechanisms are responsible for the dispersion of the scalar: molecular, mechanical, and turbulent diffusion. Modelling the transport of scalar as a stationary advection diffusion process, one can write:

$$\vec{U} \cdot \nabla C = \nabla \cdot (D \nabla C) \qquad (2)$$

where the total diffusion coefficient D accounts for the three mechanisms mentioned above.

Mechanical dispersion appears negligible at the lowest Reynolds number, as suggested by the fact that the plume has a minimum meandering motion along the centreline. Even when the plume bifurcates due to the impact on a structure ligament, it recovers its original direction immediately past the fin. The effect of the random hole distribution on the scalar pattern appears much more significant at Re=290: the plume successively bifurcates as it crosses the eight fins, fanning out in multiple branches. This is consistent with the steep increase in mechanical dispersion for Re=80 to 290 reported in Fig. 8.

At Re=458 the extent of the plume isosurface has shrunk significantly, fading away between the 5th and 7th fins. Based on the streamwise vortical structures and mechanical dispersion evolution, we hypothesized that a change in regime, i.e. the inception of an unsteady/turbulent motion occurs between Re=290 and 458, The scalar measurements corroborate this view, suggesting that turbulent dispersion starts to play a role in this range of Reynolds numbers.

At Re=1860, the 2.5% concentration isosurface is limited to the first few fins, after which turbulence is effective in diffusing the scalar to very low values of concentration. Figure 10 displays the isosurface at 0.3% for this case. With respect to the lower Reynolds number cases, the plume spreads more isotropically, and less as a tangle of branches, consistent with the diffusive nature (in the time-averaged sense) of the turbulent transport. In Fig. 10 the scalar concentration along the YZ plane half-way between fin 6 and 7 is shown. The plane is at a distance X'/d=22.8 from the origin of the plume (X' indicates the streamwise coordinate with origin at the injection location). The local signal magnitude is normalized by the maximum signal magnitude along the plane. The data, originally on a Cartesian grid, is projected by bi-cubic interpolation on polar coordinates along a circle of radius 2d, centred at the maximum concentration point (less than 1d from the channel centreline). The circle is discretized in a grid of 20 radial and 80 azimuthal nodes.

Circumferential averaging reduces the random local variation due to mechanical dispersion and noise, leading to a fairly smooth radial distribution, which can be used to determine the total diffusion coefficient in Eq. 2. Applying Taylor's theory of turbulent dispersion of a passive scalar in a flow of uniform mean velocity, one can attempt to analyze the concentration across the plume and compare it with an ideal Gaussian distribution.

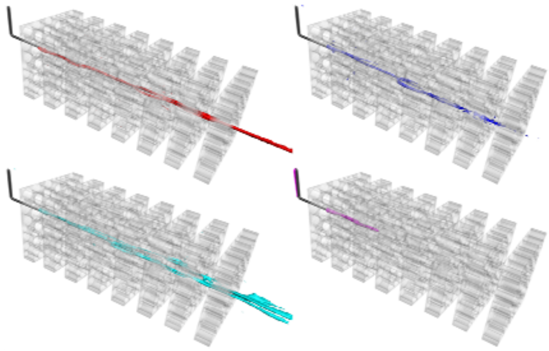

Figure 9. Isosurfaces of injected scalar at 2.5% concentration for (from top to bottom) Re=145, 290, 458 and 1860.

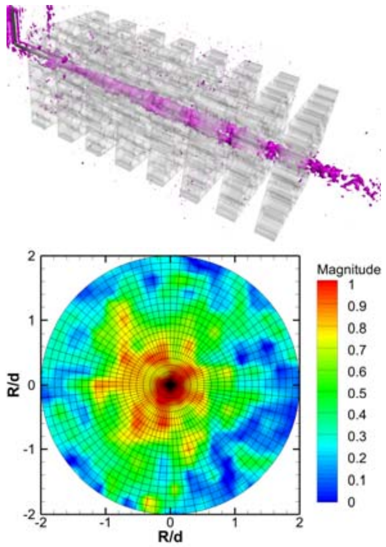

Figure 10. Left: isosurface of injected scalar at 0.3% concentration for Re=1860. Right: scalar measurements: normalized signal magnitude along a YZ plane in between fins 6 and 7, projected on a circle centered at the maximum concentration point.

Figure 11 shows radial profiles for the case at Re=1860 at various streamwise locations: half-way between fins 4 and 5, 5 and 6, 6 and 7, and 7 and 8. The good Gaussian fits indicate that the flow around the centreline behaves to a good approximation like a region of homogeneous turbulence with uniform mean velocity.

Assuming uniform mean velocity and diffusivity, Eq. 2 can be integrated leading to the following relation (similar to Eq. 1) between the standard deviation of the concentration profile σ and the diffusion coefficient:

$$\left(\frac{\sigma}{d}\right)^2 = \frac{2D}{Ud}\cdot\frac{x}{d} \qquad (3)$$

Plots of $(\sigma/d)^2$ versus x/d show the expected linear behavior (Fig. 12), from which D can be determined. Buice and Eaton (1999) followed an analogous procedure to determine the turbulent diffusivity downstream of a heated wire in a perturbed channel flow. The diffusivity coefficient estimated from the linear fit is $2.2\cdot10^{-5}$, and accounts for the molecular, mechanical and turbulent transport. Its value is about 22 times higher than the molecular viscosity of the working fluid (which is water for the Re=1860 case). The contribution of turbulent dispersion is dominant, but the mechanical dispersion (which is about 3.5 times higher than molecular viscosity, see Fig. 8) plays a non-negligible role.

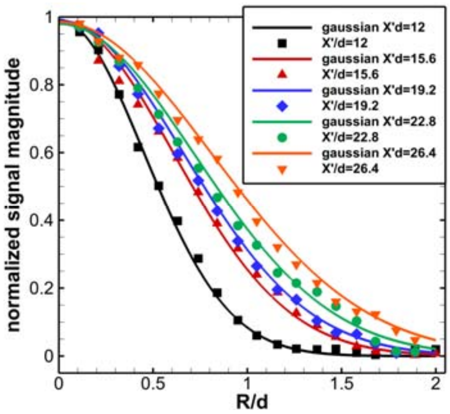

Figure 11. Scalar measurements: radial profiles of azimuthally averaged signal magnitude for various streamwise locations.

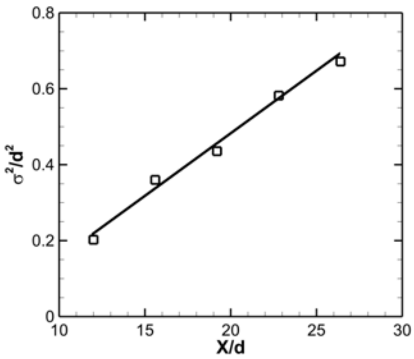

Figure 12. Variance of concentration across the scalar plume versus streamwise coordinate, fit by linear regression.

CONCLUSIONS

In the present study we combine mean velocity and mean concentration measurements to investigate the flow and scalar transport through a set of porous fins with random hole distributions. A broad spectrum of Reynolds numbers is tested, ranging from nominally laminar (Re=80) to fully turbulent (Re=3800). The velocity and vorticity fields show that the randomness of the geometry generates strong shear and mixing in the transverse plane. The interaction of colliding wall jets of different intensity and orientation leads to the formation of large streamwise swirling structures. The intensity and longevity of the vortices vary non-monotonically with the Reynolds number, peaking around Re=290.

The random distribution of holes causes a random-walk behavior, resulting in a significant mechanical dispersion. The mechanical dispersion evaluated using the mean streamline paths grows monotonically with Reynolds number, but there is a sharp change in slope for Re>290 indicating a change in flow regime.

The effect of the streamlines meandering on the concentration field is demonstrated by tracking an isokinetic non-buoyant plume of scalar injected upstream of the fin set. With increasing Reynolds number the diffusion of scalar away from the injection location is faster. This is partly due to the enhanced mechanical dispersion, and partly to the inception of unsteady/turbulent motion. The concentration data confirm that the changes occurs around Re=290. The total diffusivity is evaluated for Re=1860 and found to be 22 times higher than the molecular diffusivity but only 6 times higher than the mechanical dispersion coefficient. This indicates that the latter can play a significant role even in regimes where turbulence has already developed.

REFERENCES

M. Benson, C.J. Elkins, P.D. Mobley, M.T. Alley, and J.K. Eaton, "Three-dimensional concentration field measurements in a mixing layer using magnetic resonance imaging." Exp Fluids 49:43-55, (2010)

H. Chiba, T. Ogushi, and H. Nakajima, "Development of heat sinks for air cooling and water cooling using lotus-type porous metals." Proceedings of AJTEC2011, AJTEC2011-44108 (2011).

C. J. Elkins, M. Markl, N.J. Pelc, and J. K. Eaton, "Magnetic resonance velocimetry for mean velocity measurements in complex turbulent flows," Exp. Fluids, 34, 494 (2003).

D. L. Kock and J. F. Brady, "Dispersion in fixed beds," J. Fluid Mech., 154, 399 (1985).

K. Muramatsu, T. Ide, H. Nakajima, and J. K. Eaton, "Heat transfer performance of lotus-type porous metals," Proceedings of the ASME 2012 Summer Heat Transfer Conference, HT2012-58050 (2012).

H. Nakajima, "Fabrication, properties and applications of porous metals with directional pores," Proceedings of Japan Academy Series B, 86, 884 (2010).

A. J. Onstad, C. J. Elkins, F. Medina, R. B. Wicker, and J. K. Eaton, "Full-field measurements of flow through a scaled metal foam replica," Exp. Fluids, 50, 1571 (2011).

P. G. Saffman, "A theory of dispersion in a porous medium," J. Fluid Mech. 6, 321 (1959)

K. Vafai, A. Bejan, W. J. Minkowycz, and K. Khanafer, "A critical synthesis of pertinent models for turbulent transport through porous media", in: "Handbook of numerical heat transfer, 2nd Edition," Wiley (2006).